# Null geodesics and shadow of hairy black holes in Einstein-Maxwell-dilaton gravity

Mohaddese Heydari-Fard,[1,*] Malihe Heydari-Fard,[2,†] and Hamid Reza Sepangi[1,‡]

[1]*Department of Physics, Shahid Beheshti University, Evin 19839, Tehran, Iran*
[2]*Department of Physics, The University of Qom, 3716146611 Qom, Iran*

(Received 8 October 2021; accepted 11 May 2022; published 6 June 2022)

The timelike and null-like geodesics around compact objects are some of the best tools to classify and understand the structure of a space-time. We study the null geodesics around charged static dilaton black holes in Einstein-Maxwell-dilaton gravity. The physical parameters for nonradial geodesics, including the effective potential, effective force, radius of the photon sphere, and impact parameter, are obtained, and effects of the charge parameter and dilaton coupling constant on these quantities are studied. Possible photon motions for different values of the impact parameter are analyzed, and unstable circular orbits and unbounded orbits are plotted. These results are compared to that of Schwarzschild, Reissner-Nordström, and Gibbons-Maeda-Garfinkle-Horowitz-Strominger black holes. Also, we study the shadow cast by a dilaton black hole and investigate how the dilaton coupling affects the size of the black hole shadow. Finally, as an application of null geodesics, we calculate the deflection of light and investigate the effects of the model parameters on the bending angle.

DOI: 10.1103/PhysRevD.105.124009

## I. INTRODUCTION

Black holes are intriguing objects in our Universe. Ever since Einstein predicted their existence in general relativity (GR), the physics of black holes has attracted considerable attention. However, theoretical results alone are not complete until they are backed up with observational data. After a century of theoretical research, remarkable success has been achieved in the strong field regime around astrophysical black holes in the past few years. In addition to the discovery of gravitational waves from the merger of a black hole binary by the Virgo and LIGO collaborations [1], another important milestone is the direct observation of a supermassive black hole at the core of the M87* elliptical galaxy by the Event Horizon Telescope Collaboration [2–4], which released the first image of a black hole shadow. If the light rays get too close to a black hole, they get strongly deflected, or even move along circular orbits on the photon sphere. This strong deflection, along with the fact that nothing can come out of the black hole, makes the black hole seem like a dark disk in the sky (called the black hole shadow). The first studies of a black hole shadow for a Schwarzschild black hole and a rotating Kerr space-time were carried out in [5,6], respectively. Such studies have received significant attention in recent years and have been widely investigated in modified theories of gravity [7–25]. Therefore, the study of null geodesics around black holes would help us to understand the properties of such objects and the geometric properties of the corresponding space-times. Also, such studies are useful for calculating other related observable quantities, such as gravitational lensing and the deflection angle of light.

An effective way to understand the structure of a space-time is to study the geodesics that have exact analytical solutions. However, it is not always possible to solve the geodesic equations analytically so that numerical solutions would be in order. In such cases, one can qualitatively analyze the behavior of geodesics from the effective potential for the radial motion. The first exact solution of geodesic equations in the space-time of a Schwarzschild black hole was obtained in terms of elliptic functions by Hagihara in 1931 [26], followed by others who, over the years, have presented analytical solutions of the geodesic equations of such a metric [27–31]. Exact solutions of geodesic equations in of Schwarzschild, Kerr, Kerr–(anti–) de Sitter, Reissner-Nordström, Reissner–Nordström–(anti–)de Sitter, and Kerr-Newman space-times were studied in [32–40], respectively. In addition, the geodesic structure around black holes in modified theories of gravity has been extensively studied. For instance, the particle motion around black holes in $f(R)$ modified gravity and Horava-Lifshitz gravity was studied in [41–45]. The analysis of null geodesics in brane world scenarios and conformal Weyl gravity were considered in [46–49]. In the space-time of Born-Infeld black holes, the null geodesics were studied in [50–53]. The timelike and null-like

*m_heydarifard@sbu.ac.ir
†heydarifard@qom.ac.ir
‡hr-sepangi@sbu.ac.ir

 

geodesics in the background of quintessential black holes was considered in [54–58]. The study of geodesic structure around hairy black holes was carried out in [59,60]. For analyses of timelike and null-like geodesics in the background of wormhole geometries, see [61–63].

It is generally accepted that the theory of GR is the theory of gravity most successful in offering a correct description of the Universe, from the planetary motion to the large-scale structure. Despite these persuasive successes of GR, there are still many open problems, including inflation, dark matter, and dark energy. Also, at small scales where quantum gravity is important, there is no plausible theory of gravity. However, string theory, in a manner dictated by its low energy limit and by supplementing the usual Einstein-Hilbert action with higher-order curvature invariants, along with an extra scalar field nonminimally coupled to gravity, could open the way for quantum gravity [64]. In this regard, a well-known scenario in which a dilaton field is nonminimally coupled to the Maxwell field has been the focus of attention in the last decade and is known as the Einstein-Maxwell-dilaton (EMD) gravity. Static, spherically symmetric charged black hole solutions of the theory were initially found by Gibbons and Maeda [65] and also, independently, by Garfinkle *et al.* [66]. These solutions have the following line element:

$$ds^2 = -\left(1-\frac{r_+}{r}\right)\left(1-\frac{r_-}{r}\right)^{\frac{1-\alpha^2}{1+\alpha^2}}dt^2 + \frac{dr^2}{(1-\frac{r_+}{r})(1-\frac{r_-}{r})^{\frac{1-\alpha^2}{1+\alpha^2}}} + r^2\left(1-\frac{r_-}{r}\right)^{\frac{2\alpha^2}{1+\alpha^2}}(d\theta^2+\sin^2\theta d\phi^2), \quad (1)$$

where $\alpha$ is the dilaton coupling constant and $r_+$ and $r_-$ represent the radii of outer and inner horizons, respectively. In the special case of $\alpha = 1$ (the simplified heterotic string), the metric corresponding to the Gibbons-Maeda-Garfinkle-Horowitz-Strominger (GMGHS) black hole is given by

$$ds^2 = -\left(1-\frac{2M}{r}\right)dt^2 + \frac{dr^2}{(1-\frac{2M}{r})} + r\left(r-\frac{Q^2}{M}\right)(d\theta^2+\sin^2\theta d\phi^2), \quad (2)$$

where $M$ and $Q$ are the Arnowitt-Deser-Misner mass and the electric charge of the black hole, respectively. The geodesic structure of massive and massless particles in the space-time of a GMGHS black hole has been extensively studied. For instance, the geodesic structure of test particles and light rays around a GMGHS black hole was studied in [67–70]. Also, the null geodesics and motion of charged test particles around a magnetically charged GMGHS black hole were discussed in [71,72], respectively. The timelike and null-like geodesics around rotating dilaton black holes were considered in [73]. The geodesic structure of normal and phantom EMD black holes presented in [74] and EMD axion black holes in [75] have also been investigated. The deflection of light and shadow of charged stringy black holes was studied in [76]. Alternatively, interesting physical aspects of dilaton black holes with the metric given in Eq. (1) have been widely studied. An extension of this solution to slowly rotating dilaton black holes was carried out in [77–79]. The black hole superradiance, phase transition, and quasinormal modes of dilaton black holes were considered in [80–82]. Shadows of EMD axion black holes and charged dilaton wormholes, thin accretion disks, and black hole mergers in EMD gravity were studied in [83–89]. Also, the light deflection of EM(anti-)D black holes, using the Gauss-Bonnet theorem, was studied in [90] together with the effect of the dilaton parameter $\alpha$ on the bending of light. The motion of electric and dilatonic charged particles with arbitrary mass around dilaton black holes has also been studied [91]. However, the motion of massless particles in the space-time of dilaton black holes with arbitrary values of $\alpha$ has not been attracting as much attention. Therefore, in this paper we consider charged static dilaton black holes, study photon trajectories on the null geodesics, investigate the effects of both the dilaton coupling and charge parameter, and compare the results to that of the Schwarzschild solution and to Reissner-Nordström ($\alpha = 0$) and GMGHS ($\alpha = 1$) black holes.

The structure of the paper is as follows. In Sec. II, we briefly introduce the charged static dilaton black holes and some of their features. The radial geodesics and null geodesics with angular momentum are studied in detail in Sec. III. A study of the black hole shadow is done in Sec. IV. In Sec. V, we study the bending of light in the space-time of dilaton black holes. Finally, our conclusions are presented in Sec. VI.

## II. STATIC CHARGED DILATON BLACK HOLES IN EMD GRAVITY

The action of EMD gravity with an arbitrary dilaton coupling is given by

$$\mathcal{S} = \int d^4x\sqrt{-g}[R - 2g^{\mu\nu}\nabla_\mu\Phi\nabla_\nu\Phi - e^{-2\alpha\Phi}F_{\mu\nu}F^{\mu\nu}], \quad (3)$$

where $g$, $R$, and $\Phi$ are the metric determinant, scalar curvature, and dilaton field, respectively. Also, $F_{\mu\nu} = \partial_\mu A_\nu - \partial_\nu A_\mu$ is the strength of the Maxwell field, with $A_\mu$ being the electromagnetic vector potential. The coupling constant $\alpha$ determines the strength with which the dilaton is coupled to the Maxwell field, and without loss of generality we consider $\alpha$ to take positive values. The low energy limit of string theory corresponds to the case of $\alpha = 1$ and $\alpha = \sqrt{3}$ represents the five-dimensional Kaluza-Klein theory. Moreover, in the case of $\alpha = 0$ we obtain Einstein-Maxwell theory coupled to a scalar field where the static black hole solution is identical to the Reissner-Nordström solution of

GR. Varying action (3) with respect to metric, dilaton, and Maxwell fields results in

$$G_{\mu\nu} = 2\Big[\nabla_\mu\Phi\nabla_\nu\Phi - \frac{1}{2}g_{\mu\nu}\nabla_\rho\Phi\nabla^\rho\Phi + e^{-2\alpha\Phi}\Big(F_{\mu\rho}F^\rho_\nu - \frac{1}{4}g_{\mu\nu}F^2\Big)\Big], \tag{4}$$

$$\nabla_\mu\nabla^\mu\Phi = -\frac{\alpha}{2}e^{-2\alpha\Phi}F^2, \tag{5}$$

$$\nabla_\mu(e^{-2\alpha\Phi}F^{\mu\nu}) = 0, \tag{6}$$

where we use the shorthand notation $F^2 = F_{\rho\sigma}F^{\rho\sigma}$. As we mentioned before, the solution for a spherically symmetric static charged dilaton black hole with arbitrary values of $\alpha$ is given by [65,66]

$$ds^2 = -f(r)dt^2 + \frac{dr^2}{f(r)} + R(r)(d\theta^2 + \sin^2\theta d\phi^2), \tag{7}$$

where

$$f(r) = \Big(1 - \frac{r_+}{r}\Big)\Big(1 - \frac{r_-}{r}\Big)^{\frac{1-\alpha^2}{1+\alpha^2}} \tag{8}$$

and

$$R(r) = r^2\Big(1 - \frac{r_-}{r}\Big)^{\frac{2\alpha^2}{1+\alpha^2}}. \tag{9}$$

The behavior of the vector potential and the dilaton field is given by

$$A_t = \frac{Mv}{r}, \tag{10}$$

$$\Phi(r) = \frac{\alpha}{1+\alpha^2}\log\Big(1 - \frac{r_-}{r}\Big). \tag{11}$$

Also, the radii of the outer and inner horizons are as follows:

$$r_+ = M\Big[1 + \sqrt{1 - v^2(1-\alpha^2)}\Big], \tag{12}$$

$$r_- = \frac{M(1+\alpha^2)\Big[1 - \sqrt{[1 - v^2(1-\alpha^2)}\Big]}{(1-\alpha^2)}, \tag{13}$$

where $M$ is the mass of the black hole and $v$ denotes the ratio of the electric charge to the black hole mass, $v = \frac{Q}{M}$. Clearly, from the reality of $r_+$ and $r_-$, a constraint $1 > v^2(1-\alpha^2)$ should be imposed. Also, for all values of $\alpha$, these solutions have an event horizon at $r = r_+$, but for any nonzero value of $\alpha$ the inner horizon at $r = r_-$ is a curvature singularity. Thus, these solutions describe black holes only when $r_- < r_+$ [66]. The extremal limit of the metric, for which $r_+ = r_-$, is achieved for $Q_{\max} = M\sqrt{1+\alpha^2}$. Here, it should be mentioned that we will restrict our studies to the region $r_+ < r < \infty$ because in this region the $t$ direction, $\partial/\partial t$, is timelike and the $r$ direction, $\partial/\partial r$, is spacelike, while in the region between the two horizons, $r_- < r < r_+$, $\partial/\partial t$ is spacelike and $\partial/\partial r$ is timelike.

It is easy to see that in the limit $v = 0$, with arbitrary values of $\alpha$, we have the Schwarzschild metric with event horizon at $r_+ = 2M$ and an intrinsic singularity at $r_- = 0$. Also, in the case of $\alpha = 0$ we obtain the Reissner-Nordström space-time metric with $r_\pm = M[1 \pm \sqrt{1-v^2}]$. Although $r_-$ appears to be ill defined at $\alpha = 1$, it is well behaved in the limit of $\alpha \to 1$ and approaches a finite value. It is easy to see that, in this case, $r_+ = 2M$, $r_- = \frac{Q^2}{M}$, the metric in Eq. (7) reduces to the GMGHS metric in Eq. (2). Note that this solution is almost identical to the Schwarzschild black hole, but the difference is that areas of spheres of constant $t$ and $r$ depend on $Q$. When $r = Q^2/M$, the area approaches zero and the surface is singular. For $Q^2 \le 2M^2$ the singular surface is inside the event horizon, while for $Q^2 = 2M^2$ the surface coincides with the horizon and a transition between the black hole and naked singularity occurs [66]. The behavior of the areal radius, $\sqrt{R(r_+)}$, as a function of the dilaton coupling $\alpha$ and charge parameter $v$ is shown in Fig. 1. It is seen that the areal radius decreases with increasing $v$ and increases very slowly with increasing $\alpha$. Also, it can be seen that in the Schwarzschild case with $v = 0$ we have $\sqrt{R(r_+)} = 2M$.

The dilaton charge is defined as [65]

$$D = -r^2\Phi(r)_{,r}|_{r\to\infty} = -\frac{\alpha M\Big[1 - \sqrt{1 - v^2(1-\alpha^2)}\Big]}{(1-\alpha^2)}. \tag{14}$$

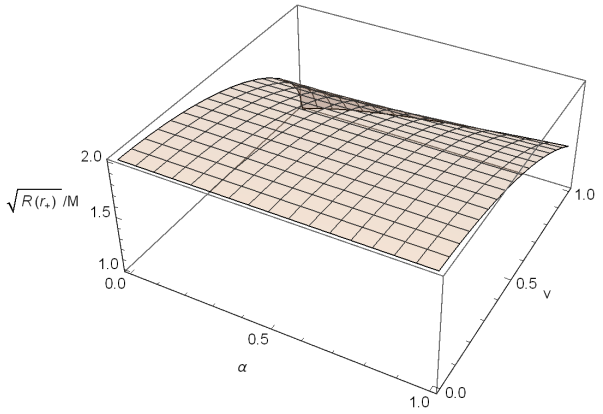


FIG. 1. Behavior of the areal radius at $r = r_+$ as a function of the charge parameter and dilaton coupling.

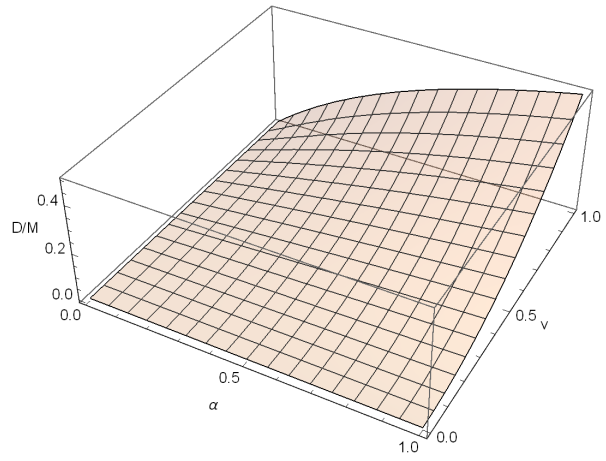


FIG. 2. Behavior of the dilaton charge as a function of the charge parameter and dilaton coupling.

We plot the behavior of the dilaton charge as a function of dilaton coupling and charge parameter in Fig. 2. As can be seen, with an increase both $v$ and $\alpha$ the dilaton charge increases. Moreover, for a Reissner-Nordström black hole with $\alpha = 0$ and Schwarzschild solution ($v = 0$) in GR, the dilaton charge is zero, as one would expect.

## III. NULL GEODESICS

In this section, we aim to investigate the geodesic structure of massless particles in the space-time of dilaton black holes. Thus, we consider the Euler-Lagrange equation

$$\frac{d}{d\tau}\left(\frac{\partial \mathcal{L}}{\partial \dot{x}^{\mu}}\right) - \frac{\partial \mathcal{L}}{\partial x^{\mu}} = 0, \tag{15}$$

where $\tau$ is the affine parameter of the light rays and the Lagrangian for the metric in Eq. (7) has the following form:

$$\begin{aligned}\mathcal{L} &= \frac{1}{2} g_{\mu\nu} \dot{x}^{\mu} \dot{x}^{\nu} \\ &= \frac{1}{2}\left(-f(r)\dot{t}^2 + \frac{\dot{r}^2}{f(r)} + R(r)(\dot{\theta}^2 + \sin^2\theta\dot{\phi}^2)\right) = 0. \end{aligned} \tag{16}$$

Since the space-time is static and spherically symmetric, we can restrict our study to the equatorial plane, $\theta = \frac{\pi}{2}$, without loss of generality. Thus, by considering $\theta = \frac{\pi}{2}$ and $\dot{\theta} = 0$, the Euler-Lagrange equations for $t$ and $\phi$ coordinates are given by

$$\dot{t} = \frac{E}{f(r)}, \tag{17}$$

$$\dot{\phi} = \frac{L}{R(r)}, \tag{18}$$

where $E$ and $L$, the energy-momentum and angular momentum of the photon, are the conserved quantities. Now, using the above equations, Lagrangian (16) takes the form

$$E^2 = \dot{r}^2 + V_{\text{eff}}(r), \tag{19}$$

where the effective potential is given by

$$V_{\text{eff}} = f(r)\frac{L^2}{R(r)}. \tag{20}$$

In order to study the path of light rays, we need the relation between $r$ and $\phi$ which can be obtained by eliminating $\tau$ from Eqs. (18) and (19),

$$\left(\frac{dr}{d\phi}\right)^2 = \frac{R^2(r)}{b^2} - R(r)f(r), \tag{21}$$

where we have substituted the effective potential from Eq. (20) and defined the impact parameter, $b \equiv \frac{L}{E}$. In particular, for light rays with a critical value of the impact parameter $b = b_c$, an unstable circular null trajectory occurs at the maxima of the effective potential $r = r_c$, known as the photon sphere [92]. In what follows, we investigate the radial null geodesics and null geodesics with angular momentum, separately.

### A. Radial null geodesics ($L = 0$)

For the radial motion with vanishing angular momentum, $L = 0$, the effective potential is zero. So, from Eqs. (17) and (19), one may find the differential equations governing the coordinate time $t$ and affine parameter $\tau$ as follows:

$$\frac{dt}{dr} = \pm\frac{1}{f(r)}, \tag{22}$$

$$\frac{d\tau}{dr} = \pm\frac{1}{E}, \tag{23}$$

where the upper and lower signs denote the outgoing and ingoing motion, respectively. Assuming photons are at $r = r_i$ when $t = \tau = 0$ and approaching $r = r_+$, we have plotted the behavior of both $t$ and $\tau$ in the space-time of a charged dilaton black hole for ingoing photons in Fig. 3. It is seen that in the affine parameter framework, the photons reach the horizon in a finite affine parameter, while for the time coordinate it takes an infinite time, which is the same behavior as that in the Schwarzschild case [32].

### B. Geodesics with angular momentum ($L \neq 0$)

Now, we will consider the angular motion of photons in the space-time around EMD black holes.

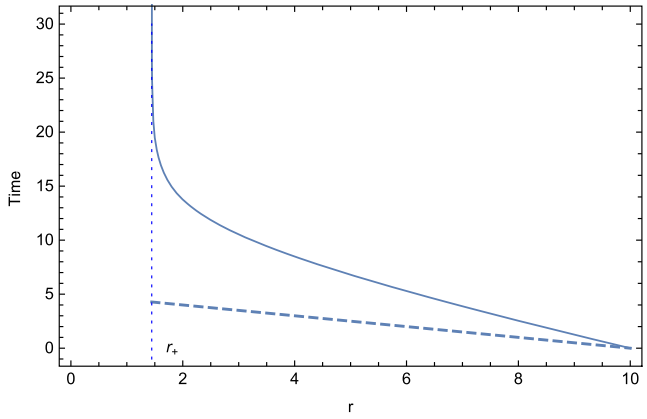


FIG. 3. The behavior of the time coordinate $t$ (solid curve) and affine parameter $\tau$ (dashed curve) as a function of radius $r$. We have set $v = 0.9$ and $\alpha = 0.1$. The vertical line represents the location of the event horizon at $r_+ = 1.44508$.

### 1. The effective potential

In this case, using Eqs. (8), (9), and (20) we find that the effective potential reads

$$V_{\text{eff}} = f(r)\frac{L^2}{R(r)} = \left(1-\frac{r_+}{r}\right)\left(1-\frac{r_-}{r}\right)^{\frac{1-3\alpha^2}{1+\alpha^2}}\frac{L^2}{r^2}. \quad (24)$$

For nonradial geodesics, it is convenient to set $L = 1$, and thus from now on we will consider $b = \frac{1}{E}$ in our calculations. We plot the effective potential in Fig. 4. In the left panel, we have shown the effect of the dilaton parameter on the potential. It is clear that by increasing $\alpha$ the maxima of effective potentials decrease such that a GMGHS black hole with $\alpha = 1$ has the lowest maximum. For different values of $v$ with a fixed value of $\alpha$, the effective potential is plotted in the right panel. It is clear that with increasing $v$ the maxima of effective potentials assume higher values. From Eq. (19), one can see that the photon motion strongly depends on its energy levels. Thus, in order to discuss various cases of motions of photons, we have shown the effective potential and some energy levels in Fig. 5. Assuming that light rays move in a radially inward direction, we summarize different kinds of motion as follows:

(1) For $b < b_c$, the photon starts at infinity and, since it does not encounter the potential barrier, falls into the black hole.
(2) The trajectories with impact parameter $b = b_c$ start falling inward from $r > r_c$ and "reach" the point $r = r_c$ only in an infinite affine time, i.e., the corresponding photons actually never reach this point but spiral with an infinite time around the photon sphere.
(3) In region 1, when $b > b_c$, the light rays that start from $r \geq r_0$ reach the potential barrier, and thus are pushed back at $r = r_0$. However, when the photon starts at $r_+ < r \leq r_1$ it will cross the horizon.

Another quantity of interest is the effective force on the photons which is given by

$$F(r) = -\frac{1}{2}\frac{dV_{\text{eff}}}{dr} = \frac{(1-\frac{r_-}{r})^{\frac{-4\alpha^2}{1+\alpha^2}}}{2r^5(1+\alpha^2)} \times [2(1+\alpha^2)r^2 - 3(1+\alpha^2)r_+ r - (3-\alpha^2)r_- r + 4r_+ r_-]. \quad (25)$$

The factor $\frac{1}{2}$ appears because of the form of Eq. (19) [54]. In Fig. 6, the total force on the photons as a function of $r$ is shown. As one expects from the shape of the potential, the effective force at the photon radius is zero. In other words, the point at which the force is zero, i.e., $r = r_c$, is important because it gives the location of the stationary point corresponding to circular geodesics. For $r_+ < r < r_c$, the force is negative and photons feel an attractive force and as a result are pulled back toward the black hole and fall into it. It is interesting to note that for $r < r_c$ the force is attractive and that is due to the fact that we are studying the configuration between $r_+$ and $r_c$. However, for $r_c < r < \infty$, the force becomes positive, driving photons away from the black hole which corresponds to photons being deflected at the turning

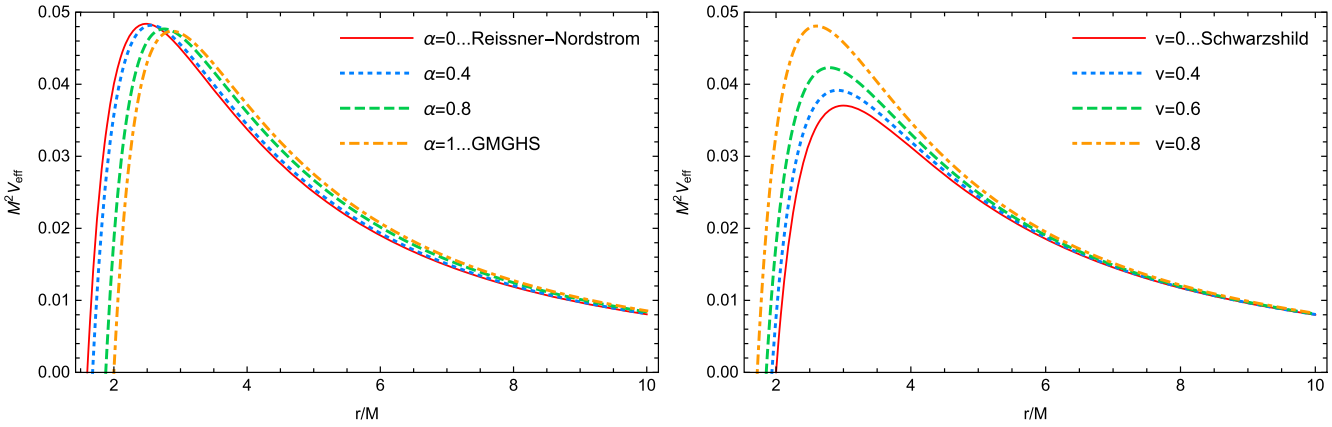


FIG. 4. The effective potential for massless particles around a static EMD black hole. In the left panel $V_{\text{eff}}$ is shown for different values of $\alpha$ with $v = 0.8$, and in the right panel for different values of $v$ for $\alpha = 0.5$.

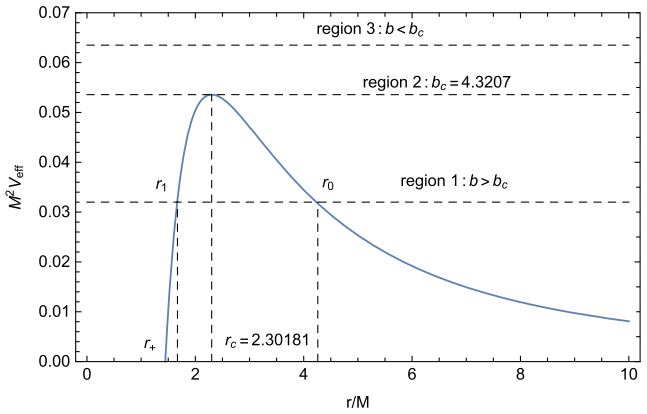


FIG. 5. The effective potential of photons around an EMD black hole and some energy levels. We set $\alpha = 0.1$ and $v = 0.9$. Region 2 corresponds to $V_{\text{eff}}(r) = 1/b_c^2$, while regions 1 and 3 correspond to $V_{\text{eff}}(r) < 1/b_c^2$ and $V_{\text{eff}}(r) > 1/b_c^2$, respectively.

point $r = r_0$. When $r \to \infty$, the force tends to zero and photons experience no force. Also, the left panel of Fig. 6 shows the effect of the dilaton parameter on the effective force. As can be seen, increasing $\alpha$ decreases the effective force. So, in the presence of dilaton hair, the force on the photon decreases such that a Reissner-Nordström black hole with $\alpha = 0$ (the scalar-free solution) has the maximum value of the force. The effect of the charge parameter on the effective force is shown in the right panel. We see that increasing $v$ also increases the effective force. Meanwhile it is easy to see that, in the limit of $\alpha \to 1$, Eq. (25) reduces to the following relation:

$$F_{GMGHS}(r) = \frac{1}{r^3(1-\frac{Q^2}{Mr})^2}\left[1 - \frac{3M}{r} - \frac{Q^2}{2Mr} + \frac{2Q^2}{r^2}\right], \quad (26)$$

which is the effective force in the space-time of a GMGHS black hole. For $Q = 0$, the above equation reduces to the effective force in the Schwarzschild space-time, that is,

$$F_{\text{Sch}}(r) = \frac{1}{r^3} - \frac{3M}{r^4}, \quad (27)$$

where the first term represents the centrifugal force and the second term corresponds to the relativistic correction due to GR [57].

### 2. Circular orbits

As mentioned in the previous section, the circular orbit occurs at $r = r_c$ with $b = b_c$, so the conditions for such a critical motion are given by

$$V_{\text{eff}} = \frac{1}{b_c^2}, \quad (28)$$

$$\frac{dV_{\text{eff}}}{dr} = 0, \quad (29)$$

which leads to the following relation:

$$R(r)f'(r) - f(r)R'(r) = 0. \quad (30)$$

The above equation has the following two solutions for circular orbit radii:

$$r_{c_\pm} = \frac{1}{2(1-\alpha^2)}\Big[3M - 2M\alpha^2 - M\alpha^2\sqrt{1 - v^2(1-\alpha^2)} \pm \sqrt{\left(3M - 2M\alpha^2 - M\alpha^2\sqrt{1 - v^2(1-\alpha^2)}\right)^2 - 8v^2(1-\alpha^2)^2}\Big]. \quad (31)$$

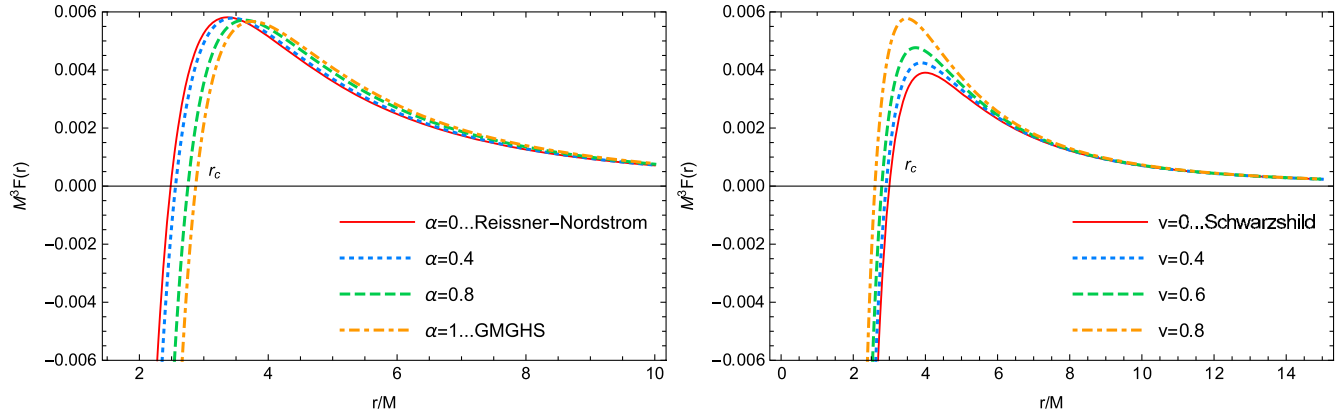


FIG. 6. Effective force as a function of $r$ for different values of $\alpha$ with $v = 0.8$ (left panel), and for different values of $v$ with $\alpha = 0.5$ (right panel).

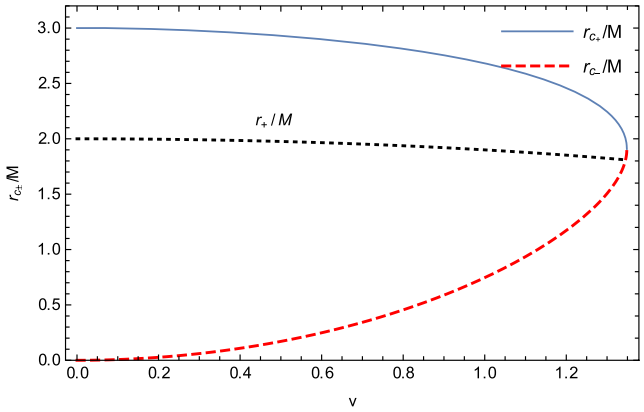


FIG. 7. Behavior of $r_{c_+}$, $r_{c_-}$, and the event horizon radius $r_+$ as a function of $v$. The dilaton parameter is set to $\alpha = 0.9$.

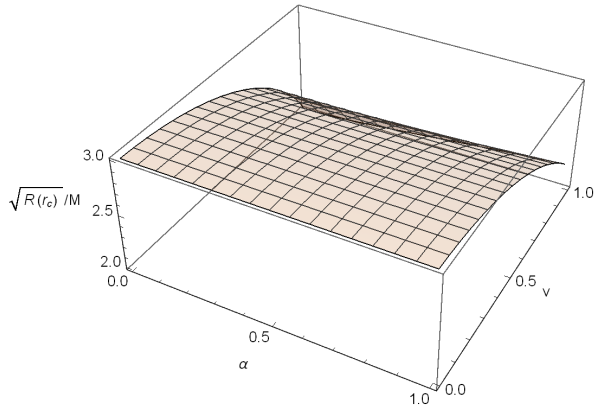


FIG. 8. Dependence of the areal radius at $r = r_c$ on the charge parameter and dilaton coupling.

We note that in the limit of $\alpha \to 1$ the above solution reduces to the radius of the circular orbit for the GMGHS black hole—namely, Eq. (49) in [68]. In Fig. 7, we display both $r_{c_+}$ and $r_{c_-}$ together with the event horizon radius as a function of $v$ for $\alpha = 0.9$. We see that for $v = 0$, $r_{c_-} = 0$ and $r_{c_+} = 3M$, which is the radius of the unstable circular orbit for the Schwarzschild black hole. Moreover, it is clear that, for all values of $v$ in Fig. 7, $r_{c_+}$ is always larger than the event horizon radius, $r_{c_+} > r_+$, while $r_{c_-}$ is smaller, $r_{c_-} < r_+$. Since we will consider the photon motion in the region $r_+ < r < \infty$, the radius denoted by $r_{c_+}$ is that of the unstable circular orbit and will be represented by $r_c$ from now on. The dependence of the areal radius at $r = r_c$ on the dilaton coupling and charge parameter is shown in Fig. 8. As can be seen, the areal radius is a decreasing function of $v$ and a very slowly increasing function of $\alpha$. Also, as is clear for an extremal Reissner-Nordström black hole with $\alpha = 0$ and $v = 1$, we have $r_c = 2M$.

TABLE I. Values of the photon radius $r_c$, the impact parameter $b_c$, and the event horizon radius for different values of $v$ with $\alpha = 0.2$. The first column with $v = 0$ corresponds to the Schwarzschild black hole.

| | $v = 0$ | $v = 0.1$ | $v = 0.3$ | $v = 0.5$ | $v = 0.7$ | $v = 0.9$ |
|---|---|---|---|---|---|---|
| $r_c/M$ | 3 | 2.9935 | 2.9406 | 2.8286 | 2.6402 | 2.3254 |
| $b_c/M$ | 5.1962 | 5.1875 | 5.1168 | 4.9681 | 4.7219 | 4.3250 |
| $r_+/M$ | 2 | 1.9952 | 1.9558 | 1.8718 | 1.7277 | 1.4716 |
| $r_-/M$ | 0 | 0.0052 | 0.0479 | 0.1389 | 0.2949 | 0.5724 |

Now, using Eqs. (19) and (20), the impact parameter of these unstable circular orbits is given by

$$b_c = \frac{L_c}{E_c} = \sqrt{\frac{R(r_c)}{f(r_c)}} = \frac{r_c}{\sqrt{(1-\frac{r_+}{r_c})(1-\frac{r_-}{r_c})^{\frac{1-3\alpha^2}{1+\alpha^2}}}}. \tag{32}$$

We present the results of the event horizon radius, photon radius, and impact parameter of the photon sphere for different values of $v$ and $\alpha$ in Tables I and II. We see that for a fixed value of $\alpha$, as one increases the charge parameter $v$, the size of the event horizon radius, photon radius, and impact parameter $b_c$ decreases. However, Table II shows that, for a given value of $v$, increasing the dilaton parameter $\alpha$ causes the event horizon radius, the photon radius, and also the value of the impact parameter to increase.

### C. Analysis of geodesics in terms of the variable $u = \frac{1}{r}$

The aim of this section is to study the geometry of null geodesics in the EMD black hole space-time. In order to do so, it is more convenient to use the variable $u = \frac{1}{r}$. Therefore, we rewrite Eq. (21) in terms of the variable $u$,

TABLE II. Values of the photon radius $r_c$, the impact parameter $b_c$, and the event horizon radius for different values of $\alpha$ with $v = 0.6$. The results in the first and sixth columns correspond to that of Reissner-Nordström and GMGHS black holes, respectively.

| | $\alpha = 0$ | $\alpha = 0.1$ | $\alpha = 0.3$ | $\alpha = 0.5$ | $\alpha = 0.7$ | $\alpha = 1$ | $\alpha = 1.3$ | $\alpha = 1.7$ | $\alpha = 2$ |
|---|---|---|---|---|---|---|---|---|---|
| $r_c/M$ | 2.7369 | 2.7391 | 2.7566 | 2.7905 | 2.8391 | 2.9343 | 3.0514 | 3.2302 | 3.3764 |
| $b_c/M$ | 4.8587 | 4.8588 | 4.8599 | 4.8619 | 4.8649 | 4.8707 | 4.8775 | 4.8877 | 4.8957 |
| $r_+/M$ | 1.8000 | 1.8023 | 1.8200 | 1.8544 | 1.9036 | 2 | 2.1173 | 2.2963 | 2.4422 |
| $r_-/M$ | 0.2000 | 0.2017 | 0.2156 | 0.2427 | 0.2818 | ⋯ | 0.4547 | 0.6098 | 0.7370 |

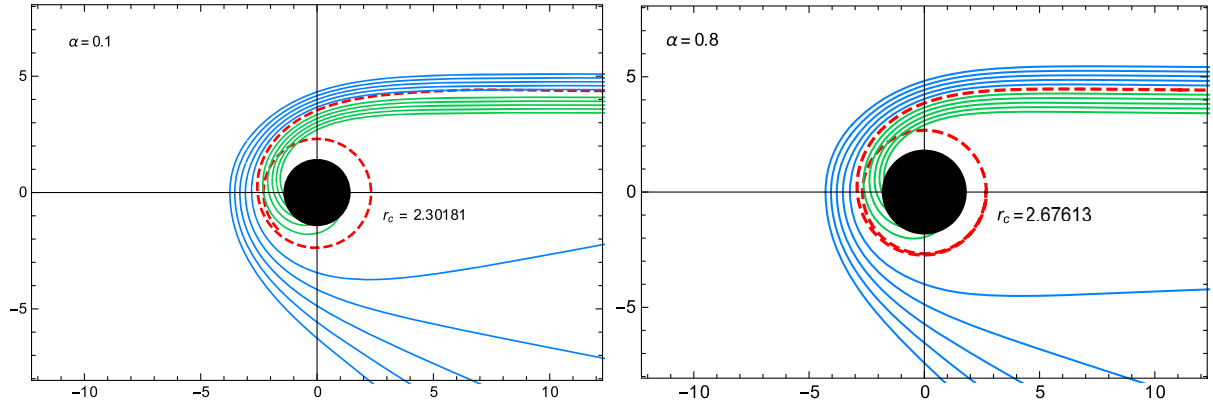


FIG. 9. Polar plot of null geodesics around an EMD black hole for $\alpha = 0.1$ and $\alpha = 0.8$ with $v = 0.9$. The red, blue, and green curves represent the null trajectories with $b = b_c$, $b > b_c$, and $b < b_c$, respectively. In each panel, a black disk shows the event horizon at $r_+ = 1.44508$ and $r_+ = 1.84167$, respectively.

$$\frac{du}{d\phi} = \sqrt{\frac{(1 - r_- u)^{\frac{4\alpha^2}{1+\alpha^2}}}{b^2} - (1 - r_+ u)(1 - r_- u)u^2} \equiv \Phi(u). \tag{33}$$

As can be seen, for $v = 0$ the above equation reduces to $(\frac{du}{d\phi})^2 = \frac{1}{b^2} + 2Mu^3 - u^2$, which is the equation of motion of photons in the space-time of the Schwarzschild black hole and, to the Reissner-Nordström black hole for $\alpha = 0$, for which it takes the form $(\frac{du}{d\phi})^2 = \frac{1}{b^2} - Q^2u^4 + 2Mu^3 - u^2$ [32]. Also, in the case of $\alpha = 1$ with metric functions given by Eq. (2), we find the corresponding result for GMGHS black holes—namely, Eq. (41) in [68].

As explained in the previous section, the photon motion depends on its energy level; see Fig. 4. When $b = b_c$, the photons have an unstable circular orbit with radius $r = r_c$ and circle the black hole on the photon sphere. However, when $b < b_c$, the light rays will continue moving inward until they are captured by the black hole. Photons with $b > b_c$ will deflect at the point $u_0 = \frac{1}{r_0}$, which is the root of the function $\Phi(u)$. In other words, the photon with $b > b_c$ reaches the turning point $u = u_0$ (or $r = r_0$) and is reflected, following an unbounded orbit. Since Eq. (33) does not have an analytical solution, we numerically plot the resulting photon paths in Fig. 9. The red curve shows photons coming from infinity and reaching the critical distance $r = r_c$, after which they revolve around the black hole on the photon sphere. However, the blue curves show the light deflection around an EMD black hole for light rays with $b > b_c$. The null geodesics falling into the black hole are shown as green curves.

## IV. SHADOW OF EMD BLACK HOLES

Let us now consider the shadow cast by dilaton black holes. To this end, it is appropriate to introduce the celestial coordinates $X$ and $Y$ as follows [6]:

$$X = \lim_{r_* \to \infty} \left( -r_*^2 \sin\theta_o \frac{d\phi}{dr} \right), \tag{34}$$

$$Y = \lim_{r_* \to \infty} \left( r_*^2 \frac{d\theta}{dr} \right), \tag{35}$$

where $r_*$ is the observer distance to the black hole and $\theta_o$ is the angular coordinate of the observer, called the inclination angle. We restrict our study to the equatorial plane $\theta_o = \frac{\pi}{2}$ so that the radius of the shadow is given by

$$R_s = \sqrt{X^2 + Y^2} = b_c. \tag{36}$$

In fact, it is found that in the particular case with $\theta_o = \frac{\pi}{2}$, for an asymptotically flat space-time with a line element in the form (7), the radius of the black hole shadow is equal to the critical impact parameter. Also, it can be seen that, for the Schwarzschild black hole, the radius of the shadow is $R_s = 3\sqrt{3} \approx 5.1962$.

In Fig. 10, we show the shadow boundaries of dilaton black holes for different values of $v$ and for changing values of the dilaton parameter $\alpha$. We see that the shape of the black hole shadow is a perfect circle and, for a fixed value of $\alpha$, the shadow size decreases when $v$ is increased. The dilaton parameter runs from $\alpha = 0$ and corresponds to a Reissner-Nordström solution, to $\alpha = 1$ in the case of a GMGHS black hole. The effect of the charge and the dilaton parameter on the shadow radius of a dilaton black hole is shown in Fig. 11. It is seen that, for a given value of $v$, the presence of the dilaton coupling $\alpha$ leads to larger values for $R_s$ than in the case of a Reissner-Nordström black hole ($\alpha = 0$) in GR. We note that the rate of increase in the shadow radius is larger for larger values of $v$. Also, for an extremal Reissner-Nordström black hole with $v = 1$, we have $R_s = 4M$. It is worth mentioning that the

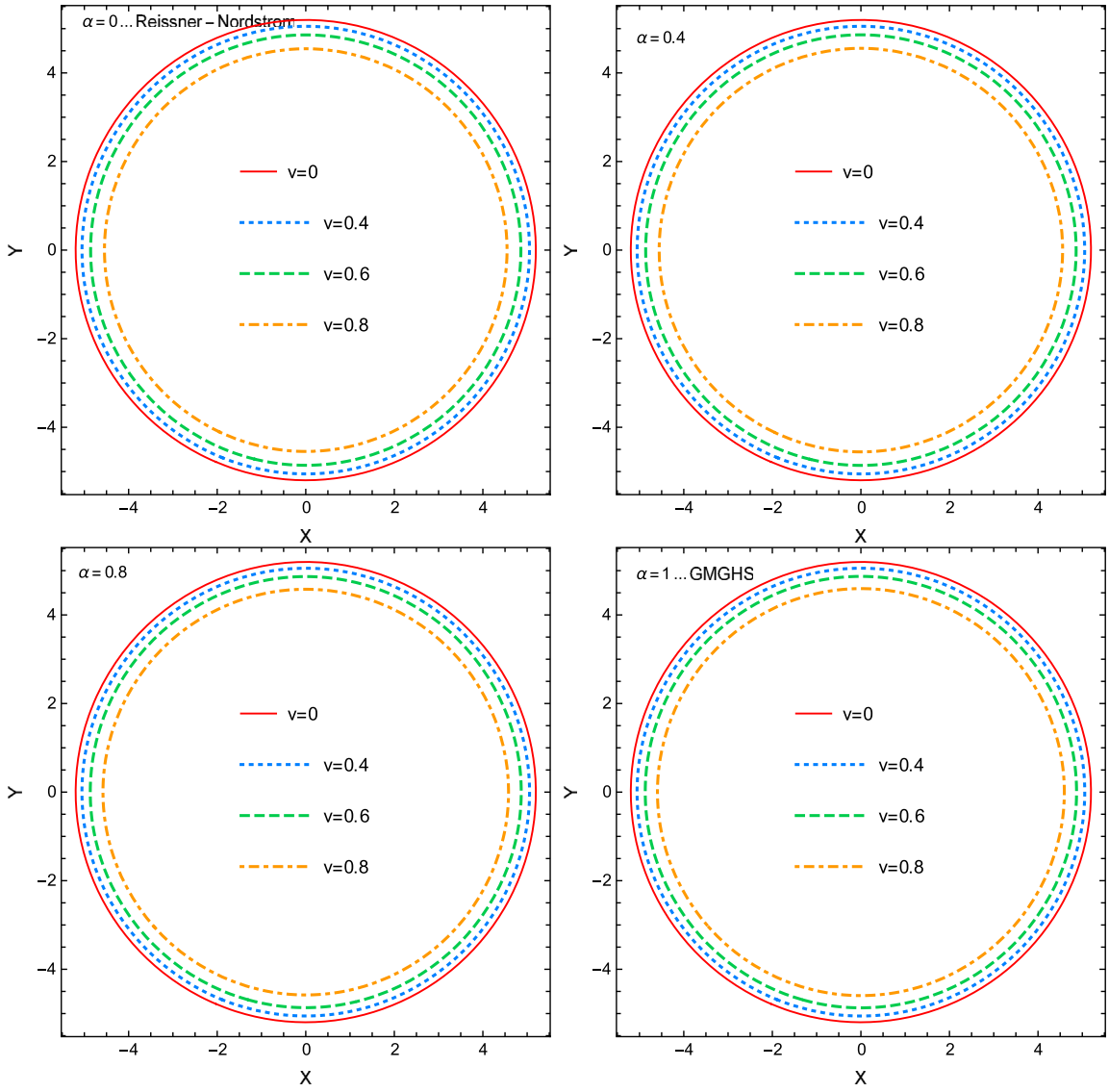


FIG. 10. Boundary of the shadow of a charged dilaton black hole for different values of the charge parameter $v$ and dilaton coupling $\alpha$. In each panel, the solid red curve shows the shadow of the Schwarzschild black hole. The unit of length along the coordinate axes $\alpha$ and $\beta$ is $M$.

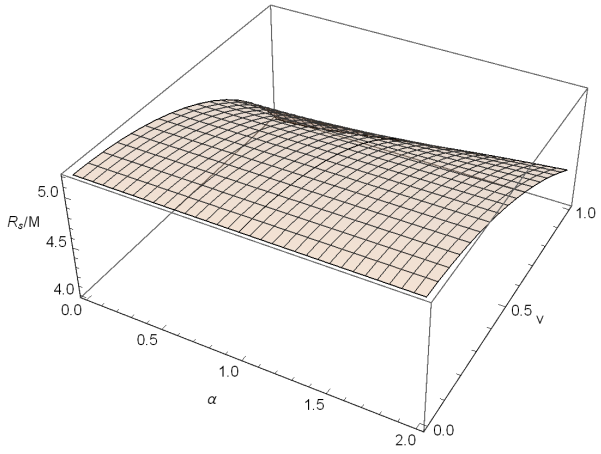


FIG. 11. Behavior of the shadow radius as a function of the charge parameter and the dilaton coupling.

measurements of the shadow size around the black hole may help to estimate the black hole parameters and probe the geometry of the background metric. However, for the EMD black holes that we are studying here, as the results in Tables I and II show, the size of the shadow, that is, $R_s = b_c$, clearly has a strong dependency on the charge parameter $v$, while the dependency on $\alpha$ seems to be quite weak. In fact, for fixed values of $v$ and values of $\alpha$ from 0 to 2, the shadow size changes by only about 0.037. Therefore, we find the effect of the dilaton parameter on the shadow size to be negligible in observational measurements.

On the other hand, astrophysical black holes are expected to have a negligible electric charge such that the charge parameter $v$ is zero or small. Therefore, it may be difficult to constrain the dilaton parameter $\alpha$ from observations of the shadow size or gravitational lensing.

## V. GRAVITATIONAL LENSING BY EMD BLACK HOLES

The study of light paths is important for investigating the gravitational lensing effects of compact objects. The problem regarding light bending in the space-time of a GMGHS black hole—and also an EM(anti-)D black hole—using the Gauss-Bonnet theorem was considered in [90]. Now, we focus on the gravitational lensing of a dilaton black hole and investigate the dependence of the bending angle on the dilaton coupling $\alpha$ and charge parameter $v$. As explained in Sec. III C, when light rays with $b > b_c$ from infinity encounter the potential barrier, they are deflected at the turning point $r = r_0$; see Fig. 4. Therefore, we first need to find the closest distance $r_0$, which is the value of $r$ when $\frac{dr}{d\phi} = 0$. From Eq. (21), we have

$$\left(\frac{dr}{d\phi}\right)^2 = \frac{r^4(1-\frac{r_\pm}{r})^{\frac{4\alpha^2}{1+\alpha^2}}}{b^2} - (r-r_+)(r-r_-) \equiv \Psi(r). \quad (37)$$

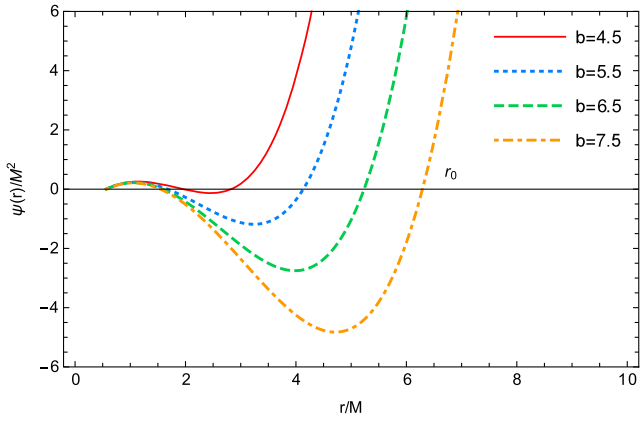


FIG. 12. Behavior of $\Psi(r)$ as a function of $r$ for different values of the impact parameter. We set $\alpha = 0.1$ and $v = 0.9$.

In Fig. 12, we display $\Psi(r)$ for different values of the impact parameter $b$. As one can see, there are two values of $r$ for which $\Psi(r) = 0$. Since we know from Fig. 4 that the value of the turning point at $r = r_0$ is larger than the photon radius at $r = r_c$, we consider the larger roots in Fig. 12 the closest distance and identify them with $r_0$. Also, we note that with an increasing impact parameter the closest distance increases as well.

Using Eq. (33), one can find the bending angle of a charged static EMD black hole according to

$$\delta = 2\int_0^{u_0}\left|\frac{d\phi}{du}\right|du - \pi = 2\int_0^{u_0}\frac{1}{\sqrt{\frac{(1-r_-u)^{\frac{4\alpha^2}{1+\alpha^2}}}{b^2} - (1-r_+u)(1-r_-u)u^2}}du - \pi, \quad (38)$$

where $u_0 = \frac{1}{r_0}$ is the inverse of the closest distance. We numerically plot the behavior of the bending angle as a function of $u_0$ in Fig. 13. In the left panel of the figure, it is clear that by increasing the dilaton coupling the bending angle also increases, so a GMGHS black hole with $\alpha = 1$ has the largest value of the deflection angle, whereas the Reissner-Nordström black hole with $\alpha = 0$ has the smallest value (see also Ref. [93]). In Table II, we see that by increasing $\alpha$ the event horizon, photon, and shadow radii increase too. This shows that increasing $\alpha$ enhances the gravitational field, and thus the deflection angle also increases with the dilaton parameter. The dependence of the bending angle on the charge parameter is presented in the right panel of Fig. 13, showing that, for a fixed value of $\alpha$, when the value of the charge parameter increases, the bending angle decreases. The corresponding results for the Reissner-Nordström and Schwarzschild black holes in GR are also plotted. Moreover, as one expects, in the limit of

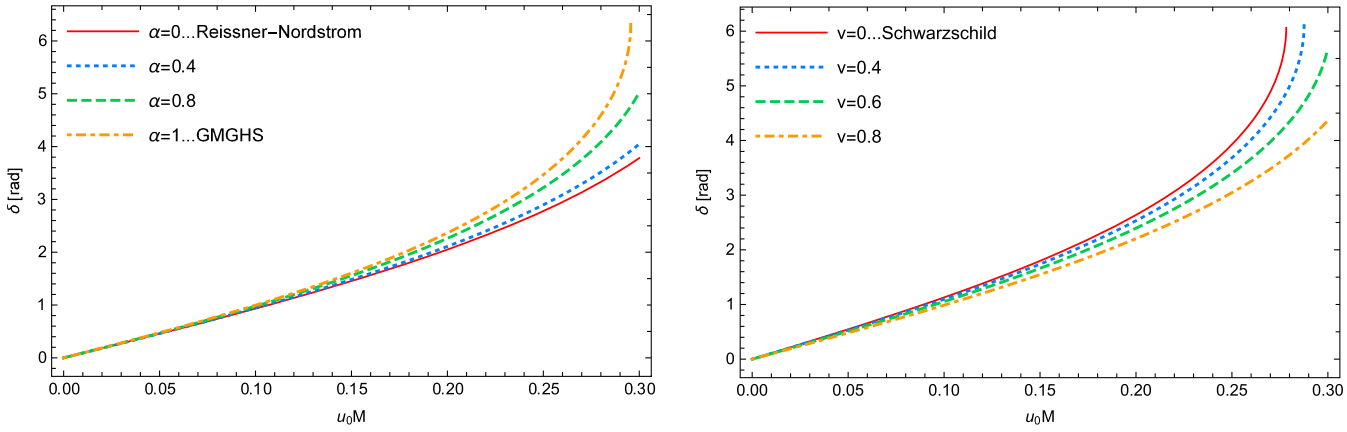


FIG. 13. Bending angle of charged static dilaton black holes as a function of the inverse of the closest distance, $u_0 = \frac{1}{r_0}$, for different values of $\alpha$ with $v = 0.9$ (left panel) and different values of $v$ with $\alpha = 0.1$ (right panel).

$u_0 \to 0$ the bending angle is zero, while for larger values of $u_0$ the deflection angle increases.

## VI. CONCLUSIONS

In this paper, we studied the null geodesics structure of charged static dilaton black holes in EMD gravity for arbitrary values of the dilaton coupling constant $\alpha$. A detailed analysis of the null geodesics around a GMGHS black hole with a specific value of $\alpha = 1$ was done previously by Fernando in [68]. However, in this work, we considered EMD black holes with arbitrary values of $\alpha$ and have investigated the effects of both the dilaton coupling and the charge parameter $v$ on the null geodesics around them. For nonradial null geodesics, we numerically obtained the effective potential, the effective force on the photons, the radius of the photon sphere, and its impact parameter. We found that, for a given value of the charge parameter, increasing the dilaton coupling $\alpha$ causes the photon radius to increase. Therefore, in the presence of dilaton hair, a black hole in EMD gravity has a larger photon radius than a Reissner-Nordström black hole (the scalar-free solution) in GR. Also, we showed that, for a fixed value of $\alpha$, by decreasing the charge parameter, the photon radius is increased such that a Schwarzschild black hole with $v = 0$ has the largest value of the photon radius.

It was also shown that, depending on the photon's energy level, there can be different kinds of motion. In this regard, by considering the incoming light rays from infinity, we discussed the possible motions of photons around EMD black holes. We showed that photons with a critical value of the impact parameter, $b_c$, move along the unstable circular orbits, while photons with $b < b_c$ eventually fall into the black hole. In a different scenario, we considered the unbounded orbits for light rays with $b > b_c$. The null trajectories of these three cases were also numerically plotted. In addition, we studied the shadow cast by charged static dilaton black holes. We found that in the presence of the dilaton coupling the size of the black hole shadow increases, while the shadow radius decreases when we increase the charge parameter. Indeed, it was shown that the shadow size has a strong dependency on the charge parameter $v$. In Table I, we see that for $\alpha = 0.2$ and a $v$ that varies from 0 to 0.9, the shadow size decreases by about 0.871. However, the dependency on the $\alpha$ parameter is very weak, as can be seen in Table II, where for a fixed value of $v = 0.6$ and an $\alpha$ that varies from 0 to 2 the size of the shadow increases by only about 0.037. It would therefore be difficult to measure the parameter $\alpha$ using observational measurements of the shadow. Finally, we studied light bending in the space-time of EMD black holes and investigated the effects of the charge parameter and dilaton coupling on the bending angle. The results were compared to dilatonic GMGHS black holes with $\alpha = 1$, a Reissner-Nordström black hole with $\alpha = 0$, and a Schwarzschild black hole in GR.


[1] B. P. Abbott *et al.* (Virgo and LIGO Scientific Collaborations), Phys. Rev. Lett. **116**, 061102 (2016).
[2] K. Akiyama *et al.*, Astrophys. J. **875**, L1 (2019).
[3] K. Akiyama *et al.*, Astrophys. J. **875**, L5 (2019).
[4] K. Akiyama *et al.*, Astrophys. J. **875**, L6 (2019).
[5] J. L. Synge, Mon. Not. R. Astron. Soc. **131**, 463 (1966).
[6] J. M. Bardeen, in *Black Holes*, Proceedings of the Les Houches Summer School, Session 215239, edited by C. De Witt and B. S. De Witt (Gordon and Breach, New York, 1973).
[7] L. Amarilla, E. F. Eiroa, and G. Giribet, Phys. Rev. D **81**, 124045 (2010).
[8] F. Atamurotov, A. Abdujabbarov, and B. Ahmedov, Astrophys. Space Sci. **348**, 179 (2013).
[9] A. Abdujabbarov, F. Atamurotov, N. Dadhich, B. Ahmedov, and Z. Stuchlik, Eur. Phys. J. C **75**, 399 (2015).
[10] P. V. P. Cunha, C. A. R. Herdeiro, B. Kleihaus, J. Kunz, and E. Radu, Phys. Lett. B **768**, 373 (2017).
[11] B. P. Singh and S. G. Ghosh, Ann. Phys. (Amsterdam) **395**, 127 (2018).
[12] S. Vagnozzi and L. Visinelli, Phys. Rev. D **100**, 024020 (2019).
[13] G. Z. Babar, A. Z. Babar, and F. Atamurotov, Eur. Phys. J. C **80**, 761 (2020).
[14] I. Banerjee, S. Chakraborty, and S. SenGupta, Phys. Rev. D **101**, 041301 (2020).
[15] X. X. Zeng and H. Q. Zhang, Eur. Phys. J. C **80**, 1058 (2020).
[16] X. X. Zeng, H. Q. Zhang, and H. Zhang, Eur. Phys. J. C **80**, 872 (2020).
[17] M. Khodadi and E. N. Saridakis, Phys. Dark Universe **32**, 100835 (2021).
[18] M. Khodadi, G. Lambiase, and D. F. Mota, J. Cosmol. Astropart. Phys. 09 (2021) 028.
[19] J. A. V. Campos, M. A. Anacleto, F. A. Brito, and E. Passos, arXiv:2103.10659.
[20] R. Shaikh, S. Paul, Pritam Banerjee, and T. Sarkar, arXiv:2105.12057.
[21] J. Badía and E. F. Eiroa, Phys. Rev. D **104**, 084055 (2021).
[22] M. Okyay and A. Övgün, J. Cosmol. Astropart. Phys. 01 (2022) 009.
[23] F. Rahaman, Ksh. Newton Singh, R. Shaikh, T. Manna, and S. Aktar, Classical Quantum Gravity **38**, 215007 (2021).
[24] M. Heydari-Fard and M. Heydari-Fard, arXiv:2109.02059.

[25] A. He, J. Tao, Y. Xue, and L. Zhang, Chin. Phys. C **46**, 065102 (2022).
[26] Y. Hagihara, Jpn. J. Astron. Geophys. **8**, 67 (1931).
[27] C. Darwin, Proc. R. Soc. A **249**, 180 (1959).
[28] C. Darwin, Proc. R. Soc. A **263**, 39 (1961).
[29] J. L. Synge, *Relativity: The General Theory* (North-Holland, Amsterdam, 1960).
[30] F. Gackstatter, Ann. Phys. (Berlin) **495**, 352 (1983).
[31] H. C. Ohanian, Am. J. Phys. **55**, 428 (1987).
[32] S. Chandrasekhar, *The Mathematical Theory of Black Holes* (Oxford University Press, New York, 1998).
[33] D. Pugliese, H. Quevedo, and R. Ruffini, Phys. Rev. D **84**, 044030 (2011).
[34] E. Hackmann, C. Lammerzahl, V. Kagramanova, and J. Kunz, Phys. Rev. D **81**, 044020 (2010).
[35] G. V. Kraniotis, Classical Quantum Gravity **21**, 4743 (2004).
[36] D. Pugliese, H. Quevedo, and R. Ruffini, Phys. Rev. D **83**, 104052 (2011).
[37] S. Grunau and V. Kagramanova, Phys. Rev. D **83**, 044009 (2011).
[38] G. Eskin, Rev. Math. Phys. **31**, 1950021 (2019).
[39] M. Olivares, J. Saavedra, C. Leiva, and J. R. Villanueva, Mod. Phys. Lett. A **26**, 2923 (2011).
[40] E. Hackmann and H. Xu, Phys. Rev. D **87**, 124030 (2013).
[41] S. Soroushfar, R. Saffari, J. Kunz, and C. Lämmerzahl, Phys. Rev. D **92**, 044010 (2015).
[42] J. Chen and Y. Wang, Int. J. Mod. Phys. A **25**, 1439 (2010).
[43] V. Enolskii, B. Hartmann, V. Kagramanova, J. Kunz, C. Lämmerzahl, and P. Sirimachan, Phys. Rev. D **84**, 084011 (2011).
[44] A. E. Mosaffa, Phys. Rev. D **83**, 124006 (2011).
[45] S. W. Wei, J. Yang, and Y. Liu, Phys. Rev. D **99**, 104016 (2019).
[46] D. Youm, Mod. Phys. Lett. A **16**, 2371 (2001).
[47] W. S. Klën and C. Molina, Phys. Rev. D **102**, 104051 (2020).
[48] B. Hoseini, R. Saffari, and S. Soroushfar, Classical Quantum Gravity **34**, 055004 (2017).
[49] J. R. Villanueva, F. Tapia, M. Molina, and M. Olivares, Eur. Phys. J. C **78**, 853 (2018).
[50] N. Breton, Classical Quantum Gravity **19**, 601 (2002).
[51] S. Fernando, ISRN Math. Phys. **2012**, 869069 (2012).
[52] A. S. Habibina and H. S. Ramadhan, Phys. Rev. D **101**, 124036 (2020).
[53] M. A. A. Paula, L. C. S. Leite, and L. C. B. Crispino, Phys. Rev. D **102**, 104033 (2020).
[54] S. Fernando, Gen. Relativ. Gravit. **44**, 1857 (2012).
[55] B. Malakolkalami and K. Ghaderi, Mod. Phys. Lett. A **30**, 1550049 (2015).
[56] R. Uniyal, D. C. Devi, H. Nandan, and K. D. Purohit, Gen. Relativ. Gravit. **47**, 16 (2015).
[57] S. Fernando, S. Meadows, and K. Reis, Int. J. Theor. Phys. **54**, 3634 (2015).
[58] K. Nozari and M. Hajebrahimi, arXiv:2004.14775.
[59] S. Hod, Phys. Rev. D **84**, 124030 (2011).
[60] A. Ramos, C. Arias, R. Ávalos, and E. Contreras, Ann. Phys. (Amsterdam) **431**, 168557 (2021).
[61] A. Mishra and S. Chakraborty, Eur. Phys. J. C **78**, 374 (2018).
[62] F. Willenborg, S. Grunau, B. Kleihaus, and J. Kunz, Phys. Rev. D **97**, 124002 (2018).
[63] I. Potashov, J. Tchemarina, and A. Tsirulev, Universe **6**, 183 (2020).
[64] M. B. Green, J. H. Schwartz, and E. Witten, *Superstring Theory* (Cambridge University Press, Cambridge, England, 1987).
[65] G. W. Gibbons and K. Maeda, Nucl. Phys. **B298**, 741 (1988).
[66] D. Garfinkle, G. Horowitz, and A. Strominger, Phys. Rev. D **43**, 3140 (1991).
[67] S. Fernando, D. Krug, and C. Curry, Gen. Relativ. Gravit. **35**, 1243 (2003).
[68] S. Fernando, Phys. Rev. D **85**, 024033 (2012).
[69] C. Blaga, Appl. Math. **22**, 41 (2013).
[70] B. Turimov, J. Rayimbaev, A. Abdujabbarov, B. Ahmedov, and Z. Stuchlík, Phys. Rev. D **102**, 064052 (2020).
[71] R. S. Kuniyal, R. Uniyal, H. Nandan, and K. D. Purohit, Gen. Relativ. Gravit. **48**, 46 (2016).
[72] P. A. Gonzalez, M. Olivares, E. Papantonopoulos, J. Saavedra, and Y. Vasquez, Phys. Rev. D **95**, 104052 (2017).
[73] S. Soroushfar, R. Saffari, and E. Sahami, Phys. Rev. D **94**, 024010 (2016).
[74] M. Azreg-Aïnou, Phys. Rev. D **87**, 024012 (2013).
[75] K. Flathmann and S. Grunau, Phys. Rev. D **92**, 104027 (2015).
[76] S. Kala, Saurabh, H. Nandan, and P. Sharma, Int. J. Mod. Phys. A **35**, 2050177 (2020).
[77] K. Shiraishi, Phys. Lett. A **166**, 298 (1992).
[78] J. H. Horne and G. T. Horowitz, Phys. Rev. D **46**, 1340 (1992).
[79] A. Sen, Phys. Rev. Lett. **69**, 1006 (1992).
[80] J. Koga and K. Maeda, Phys. Lett. B **340**, 29 (1994).
[81] S. H. Hendi, A. Sheykhi, S. Panahiyan, and B. Eslam Panah, Phys. Rev. D **92**, 064028 (2015).
[82] C. Pacilio and R. Brito, Phys. Rev. D **98**, 104042 (2018).
[83] S. W. Wei and Y. X. Liu, J. Cosmol. Astropart. Phys. 11 (2013) 063.
[84] L. Amarilla and E. F. Eiroa, Phys. Rev. D **87**, 044057 (2013).
[85] M. Amir, A. Banerjee, and S. D. Maharaj, Ann. Phys. (Amsterdam) **400**, 198 (2019).
[86] R. Kh. Karimov, R. N. Izmailov, A. Bhattacharya, and K. K. Nandi, Eur. Phys. J. C **78**, 788 (2018).
[87] M. Heydari-Fard, M. Heydari-Fard, and H. R. Sepangi, Eur. Phys. J. C **80**, 351 (2020).
[88] P. Jai-akson, A. Chatrabhuti, O. Evnin, and L. Lehnerc, Phys. Rev. D **96**, 044031 (2017).
[89] E. W. Hirschmann, L. Lehner, S. L. Liebling, and C. Palenzuela, Phys. Rev. D **97**, 064032 (2018).
[90] A. Ovgun, G. Gyulchev, and K. Jusufi, Ann. Phys. (Amsterdam) **406**, 152 (2019).
[91] T. Maki and K. Shiraishi, Classical Quantum Gravity **11**, 227 (1994).
[92] C. M. Claudel, K. S. Virbhadra, and G. F. R. Ellis, J. Math. Phys. (N.Y.) **42**, 818 (2001).
[93] G. N. Gyulchev and S. S. Yazadjiev, SFIN A **1**, 229 (2006).